Published in final edited form as:
Cancer Res. 2017 June 01; 77(11): 2903–2913. doi:10.1158/0008-5472.CAN-16-3044.

Metabolic Markers and Statistical Prediction of Serous Ovarian Cancer Aggressiveness by Ambient Ionization Mass Spectrometry Imaging

Marta Sans[1], **Kshipra Gharpure**[2], **Robert Tibshirani**[3], **Jialing Zhang**[1], **Li Liang**[4], **Jinsong Liu**[4], **Jonathan H. Young**[1], **Robert L. Dood**[2], **Anil K. Sood**[2,5,6,*], and **Livia S. Eberlin**[1,*]

[1]Department of Chemistry, The University of Texas at Austin, Austin, TX, 78712

[2]Department of Gynecologic Oncology, The University of Texas MD Anderson Cancer Center, Houston, TX, 77030

[3]Departments of Biomedical Data Sciences and Statistics, Stanford University, Stanford, CA 94305

[4]Department of Pathology, The University of Texas MD Anderson Cancer Center, Houston, TX, 77030

[5]Department of Cancer Biology, The University of Texas MD Anderson Cancer Center, Houston, TX, 77030

[6]Center for RNA Interference and Non-Coding RNA, The University of Texas MD Anderson Cancer Center, Houston, TX, 77030

Abstract

Ovarian high-grade serous carcinoma (HGSC) results in the highest mortality among gynecological cancers, developing rapidly and aggressively. Dissimilarly, serous borderline ovarian tumors (BOT) can progress into low-grade serous carcinomas and have relatively indolent clinical behavior. The underlying biological differences between HGSC and BOT call for accurate diagnostic methodologies and tailored treatment options, and identification of molecular markers of aggressiveness could provide valuable biochemical insights and improve disease management. Here we used desorption electrospray ionization (DESI) mass spectrometry (MS) to image and chemically characterize the metabolic profiles of HGSC, BOT, and normal ovarian tissue samples. DESI-MS imaging enabled clear visualization of fine papillary branches in serous BOT and allowed for characterization of spatial features of tumor heterogeneity such as adjacent necrosis and stroma in HGSC. Predictive markers of cancer aggressiveness were identified, including various free fatty acids, metabolites, and complex lipids such as ceramides, glycerophosphoglycerols, cardiolipins, and glycerophosphocholines. Classification models built from a total of 89,826 individual pixels, acquired in positive and negative ion modes from 78 different tissue samples, enabled diagnosis and prediction of HGSC and all tumor samples in comparison to normal tissues, with overall agreements of 96.4% and 96.2%, respectively. HGSC

---

[*]to whom correspondence should be addressed: asood@mdanderson.org, liviase@utexas.edu.

Conflict of Interest: The authors declare that there is no conflict of interest.

and BOT discrimination was achieved with an overall accuracy of 93.0%. Interestingly, our classification model allowed identification of three BOT samples presenting unusual histologic features that could be associated with the development of low-grade carcinomas. Our results suggest DESI-MS as a powerful approach for rapid serous ovarian cancer diagnosis based on altered metabolic signatures.

Introduction

Epithelial ovarian cancer is a complex disease that includes great molecular and histological diversity, with serous carcinoma being the most common form (1). Ovarian cancer accounts for the majority of deaths for gynecological malignancies due to the detection of advanced and aggressive disease at a late stage (2). High-grade serous cancer (HGSC) is the most aggressive ovarian epithelial cancer and accounts for 70% of all ovarian epithelial cancers diagnosed (3). HGSC is characterized by extensive genetic instability and TP53 mutations are universally found in these tumors (4). Conversely, borderline serous ovarian tumors (BOT) or serous tumors of low-malignant potential are non-invasive neoplasms with favorable patient prognosis, and represent approximately 15% of serous ovarian tumors (5). BOTs can progress to malignant low-grade serous carcinoma (LGSC), but the clinical outcome is still advantageous in comparison to HGSCs (4,6). HGSC and BOTs present distinct tumor invasion behaviors, with HGSC growing rapidly and spreading among healthy tissue, while BOTs slowly proliferate without stromal invasion. Although histopathologic analysis is routinely employed for diagnosis of serous ovarian tumors, sensitive methods that provide molecular information to diagnose and stratify patients could serve as complimentary tools for more accurate and personalized diagnosis, as well as for the detection of early molecular markers to improve disease management (7–9). Moreover, characterization of the molecular differences between malignant and borderline serous ovarian tumors could provide new insights to unravel the biological mechanisms driving tumor invasion and aggressiveness (10,11).

Mass spectrometry imaging techniques have been increasingly used for spatial and molecular characterization of cancerous tissues (12–14). In particular, desorption electrospray ionization mass spectrometry (DESI-MS) imaging allows simultaneous detection of hundreds of lipids and metabolites directly from tissue samples with minimal sample preparation (15). DESI-MS employs an electrospray stream to desorb and ionize molecular species present on the sample surface (16). When performed in the imaging mode, chemical maps displaying the spatial distribution of molecular ions are obtained (17). Multivariate statistical analysis of the large spatial and molecular data information obtained is essential to derive molecular signatures that are predictive of disease state. DESI-MS imaging is powerful for biomarker discovery as it allows visualization of tissue heterogeneity and thus unambiguous correlation of histologic features and molecular information to build tissue-based molecular classifiers. This methodology has been used to investigate diagnostic lipid and metabolic signatures of human cancerous tissues including brain (18), breast (19), gastric (20), and others (21–23). Mouse models of human ovarian HGSC have been recently investigated using DESI-MS imaging, and differences in metabolic species were observed between healthy and tumorous tissues (24).

Here, we report the use of DESI-MS imaging to investigate the molecular profiles of serous ovarian tumors and characterize lipids and metabolites that could potentially serve as markers of aggressive disease. 2D molecular images allowed correlation between molecular signatures and regions with specific histological features. Classification models built using the least absolute shrinkage and selector operator (Lasso) technique (25,26) were tested to predict disease state and tumor aggressiveness. Predictive species selected by the statistical models were tentatively identified by high mass accuracy/high mass resolution and tandem mass spectrometry analysis as lipids and metabolites of biological relevance. Our results demonstrate the capabilities of DESI-MS characterizing serous ovarian tumors and for the identification of potential predictive markers of disease aggressiveness.

Materials and Methods

Banked Human Ovarian Tissues

A total of 78 frozen human tissue specimens including 15 normal ovarian tissues, 15 BOT, and 48 HGSC samples were obtained from the Cooperative Human Tissue Network and MD Anderson Tissue Bank under approved IRB protocol. Tissue samples were sectioned at 16 μm thick sections using a CryoStar™ NX50 cryostat (Thermo Scientific, San Jose, CA). After sectioning, the glass slides were stored in a −80°C freezer. Prior to MS imaging, the glass slides were dried for ~15 min.

DESI-MS imaging

A 2D Omni Spray (Prosolia Inc., Indianapolis, IN) coupled to an LTQ-Orbitrap Elite was utilized for tissue imaging. DESI-MS imaging was performed in the negative and positive ion modes from *m/z* 100-1500, using a hybrid mass spectrometer which allows for tandem MS experiments, high mass accuracy (<5 ppm mass error) and high mass resolution (60,000 resolving power) measurements. The spatial resolution was of 200 μm. Ion images were assembled using Biomap and MSiReader software. The histologically compatible solvent system dimethylformamide: acetonitrile (DMF:ACN) 1:1 (v/v) was used for negative ion mode analysis, at a flow rate of 1.2 μL/min (27). For positive ion mode analysis, pure ACN was used, at a flow rate of 3 μL/min. The N_2 pressure was set to 185 psi. For ion identification, high mass resolution/accuracy measurements using the same tissue sections analyzed were conducted using CID and HCD methods, using the Orbitrap for analysis.

Histopathology and light microscopy

The same tissue sections analyzed by DESI-MS imaging were subjected afterwards to standard H&E staining protocol. Pathologic evaluation was performed by Dr. Jinsong Liu and Dr. Li Liang using light microscopy. Regions of clear diagnosis were assigned and delineated in the glass slides. Light microscopy images of the H&E stained slides were taking using the EVOS FL Auto Cell Imaging System (Invitrogen, Thermo Fisher Scientific, Waltham, Massachusetts, USA).

Statistical Analysis

MS data corresponding to the areas of interest was extracted from the ion images using MSiReader software. The *m/z* range was discretized by performing hierarchical clustering and cutting the resulting dendrogram at distance 0.05. Peaks appearing in more than 10% of the pixels were kept for analysis. For two-class classification (normal vs HGSC, and HGSC vs BOT), logistic regression was performed with Lasso regularization using the “glmnet” package (26) in the R language. Regularization parameters were determined by 3-fold cross-validation analysis. The data was randomly divided in a training and validation set of samples, 50-50 per patient basis. For 3 class classification (normal vs BOT vs HGSC), a customized training approach was employed as previously described (28).

Results

Molecular imaging of serous ovarian cancers

DESI-MS imaging was performed in the negative and positive ion modes for a total of 78 tissue samples, including 15 normal ovarian, 15 BOT and 48 HGSC tissues obtained from two independent tissue banks. A patient demographic table is included in Supplemental Table 1. Characteristic metabolic profiles for HGSC, serous BOT, and normal ovary samples were observed in both polarities and presented a remarkable diversity of metabolic species. In the negative ion mode, small metabolites, saturated and unsaturated fatty acids, sphingolipids (SP), and several classes of glycerophospholipids (GP) such as ceramides (Cer); cardiolipins (CL), glycerophosphoethanolamines (PE), glycerophosphoglycerols (PG), glycerophosphoserines (PS) and glycerophosphoinositols (PI) were observed (Figure 1A), while additional biologically relevant lipid species, such as glycerophosphocholines (PC), triacylgycerols (TG) and sphingomyelins (SM) were seen in the positive ion mode (Figure 2A).

After DESI-MS imaging, the same tissue sections were stained with H&E and subjected to detailed pathologic evaluation (27). Specific histologic features characteristic of HGSC and serous BOT tissues were observed and annotated for all samples analyzed, as shown in Figure 1 and Figure 2 for four representative samples for negative and positive ion mode, respectively. HGSCs exhibit solid growth or large and complex papillae, with heterogeneous nuclei shape and sizes, and extensive stromal invasion (1,4). DESI-MS imaging in the negative ion mode allowed visualization of regions with tumor clusters in HGSC, as outlined in black for samples HGSC_9 and HGSC_11 in Figure 1B. For example, high relative abundances of *m/z* 885.547, *m/z* 747.516, *m/z* 724.484, and *m/z* 281.248 were observed in regions with high density of tumor cells. In the positive ion mode, PC species including PC 36:3, PC 34:1 and PC 32:1 were found at high relative abundances in high-grade carcinoma regions, allowing clear visualization of these regions in comparison to surrounding stroma. Interestingly, *m/z* 901.648, tentatively identified as ubiquinone or Coenzyme Q10 with a mass error of −1.1 ppm, was noticeably selective to the presence of tumor in HGSC samples (Figure 2B).

Conversely, serous BOTs are commonly associated with non-invasive components, characterized by increased epithelial proliferation and nuclear atypia, exhibiting multiple papillae with ordered branching (5,6). Serous BOT samples present a distinct histological architecture characterized by tumor growth within the lining of the stroma. Ion images of serous BOT samples BOT _4 and BOT_16 are shown in Figure 1C and Figure 2C. As observed for HGSC samples, high relative abundance of PI 18:0/20:4 was seen in the tumor region in comparison to stromal areas. Yet, high relative abundances of ceramide species such as Cer d42:1, Cer d42:2, Cer d40:1 and Cer d34:1 was highly specific to the discrete tumor regions in BOT samples. In the positive ion mode, ubiquinone (*m/z* 901.648) also presented higher relative abundances in serous BOT regions. Other species such as PC 36:3 or 36:4 were also abundant within the tissue slides but not as specific to the BOT tumor areas. On the other hand, cholesteryl ester (CE) 18:2 was observed to be more abundant in the surrounding stromal regions.

Normal ovarian tissue samples presented stromal regions with heterogeneous features such as corpus luteum, follicles or benign cysts (Supplemental Figure 1). Healthy stromal ovarian tissue consistently displayed a lower overall signal intensity for lipid species when compared to HGSC tissue samples in the negative ion mode. Moreover, a higher relative abundance of PI 20:4/18:1, *m/z* 885.547, in comparison to PS 18:0/18:1, *m/z* 788.547, was consistently observed in both BOT and HGSC tumors, when compared to normal ovarian tissues. However, certain species, such as ascorbic acid, *m/z* 175.025, were more prominent in normal tissue. In the positive ion mode, characteristic mass spectra were observed from normal stromal regions, with high relative abundance of PCs such as PC 34:1, and other less abundant lipid species such as PC 36:1 or diacylglycerol (DG) 28:4.

Notably, the spatial resolution used for DESI-MS imaging (200 μm) enabled visualization of key features of tumor heterogeneity in serous ovarian tumor tissues. Figure 3 shows magnified regions for three tumor samples; with selected ion images which directly correlate and clearly outline histological details of these tissues. For example, necrotic regions within the HGSC_1 tissue sample (outlined in red Figure 3C) showed a very distinct lipid profile, characterized by high relative abundance of ceramide species such as *m/z* 682.591 and *m/z* 600.513 (Supplemental Figure 2). Necrosis is a typical cell injury present in high-grade carcinomas, and was absent in BOT tumors (1,4). In HGSC and BOT samples, the molecular composition of tumor regions allowed clear visualization and discrimination of cancer and adjacent stromal regions. The distinct molecular compositions associated to normal ovarian tissues, and borderline and high-grade tumors strongly suggest lipid and metabolite species as potential biomarkers for cancer diagnosis and aggressiveness.

Statistical prediction and molecular diagnosis of HGSC

DESI-MS imaging of tissue samples results in a large amount of molecular and spatial information (hundreds of molecular ions/hundreds of data points/sample) and thus calls for refined statistical evaluation to define what changes in molecular expression are significantly different between phenotypes and to build robust statistical classifiers. The Lasso method was performed on a random training set of samples to yield a model with parsimonious sets of *m/z* values for discriminating between the classes. A mathematical weight for each mass spectral feature was calculated by the Lasso depending on the importance that the feature had in characterizing a certain class. The predictive accuracy of the model with the selected features was evaluated using an independent validation set, and presented as agreement (%) with pathological results.

To classify HGSC pixels in comparison to normal tissue, MS data was extracted from tumor concentrated regions or stromal areas within the selected tissues slides. First, we built a classifier for HGSC using a training subset of samples (8 normal, 23 HGSC). Three-fold cross-validation (CV) was performed on a pixel-by-pixel basis using a total of 20,082 pixels evaluated in the negative ion mode, resulting in an overall agreement of 97.1%. The statistical model was then applied to the validation set of samples (7 normal, 25 HGSC) which resulted in an overall agreement of 96.5% for 18,671 pixels (Figure 4A). The area under the curve values (AUC=0.98 for cross validation, AUC=0.97 for validation set) demonstrate the high performance for normal versus HGSC discrimination. Analysis per patient allowed correct classification of 100% of the patients in CV, while 1 HG sample was misclassified as normal out of the total 25 validation set samples (Supplemental Table 2). A subset of 25 *m/z* values selected by the Lasso as most significant contributors to the model were tentatively identified as small metabolites, saturated and polyunsaturated fatty acids, and GPs (Supplemental Table 3). The positive ion mode data was also analyzed by the Lasso to predict HGSC. Following the same strategy, overall agreements of 96.7% (AUC=0.96) and 95.5% (AUC=0.95) for CV and validation sets were achieved, respectively (Figure 4B). The Lasso selected 21 *m/z* values characteristic for the model, the majority of which were identified as PCs, CEs, and TGs (Supplemental Table 3). These results demonstrate DESI-MS and Lasso's capabilities of diagnosing the most aggressive form of serous ovarian cancers, which is relevant due to the high occurrence and poor prognosis of HGSC compared to other subtypes (4).

Statistical prediction of cancer aggressiveness for HGSC and BOT tissues

HGSC and BOT tumors present very distinct behaviors including tumor invasion and aggressiveness. Investigating the molecular differences between HGSC and BOT subtypes can assist in the identification of potential biomarkers of disease aggressiveness. Molecular classifiers to predict BOT and HGSC were built using the Lasso for DESI-MS data. In the negative ion mode, the classifier was developed using a training set of samples (32 samples, 18,190 pixels) resulting in an overall agreement of 93.2% with pathologic analysis by cross-validation. The remaining data (31 samples, 13,422 pixels) used to test the molecular model yielded 91.8% agreement with evaluation by pathology. Using positive ion mode data, agreements of 90.4% (29 samples, 20,852 pixels) and 97.5% (32 samples, 15,134) were obtained for the training and test sets, respectively (Supplemental Table 4). From the species selected as predictive markers by the molecular classifier, 41 *m/z* values were identified as metabolites, fatty acids, complex sphingolipids or glycerophospholipids in the negative and positive ion modes (Supplemental Table 5).

Per patient analysis revealed 3 BOT samples misclassified overall: BOT_2, BOT_6 and BOT_13, which were then re-evaluated by pathology (Supplemental Table 4). Remarkably, invasive carcinoma features were identified within the tissue sample for BOT_2, which are commonly associated with the development of LGSC. The surgical report for BOT_6 revealed that the patient's contralateral ovary consisted of well-differentiated (low-grade) adenocarcinoma, indicative of malignant behavior. Samples BOT_6 and BOT_13 were defined by pathology as serous BOT with unusual extensive micropapillary growth patterns and architectural complexities, thus supporting the distinct molecular features detected by DESI-MS that are not characteristic of the BOT molecular model.

Statistical prediction of serous ovarian cancers and normal ovarian tissues

Next, we evaluated the ability of our method to discriminate three classes of ovarian tissues; normal, BOT and HGSC. Lasso was performed on negative ion mode DESI-MS data from 15 normal, 15 BOT and 48 HGSC tissue samples. A customized training approach was utilized to provide localized molecular models for predicting each data subset, which has been previously applied to MS imaging data (28). A total of 20,225 pixels (39 samples) were used for CV leading to an overall agreement of 92.5%. The remaining 22,513 pixels (39 samples) were evaluated as an independent validation set with an overall 88.6% agreement (Figure 4A). Positive ion mode analysis from a total of 10 normal, 15 BOT and 46 HGSC tissue samples, provided an overall agreement of 91.0% in CV (25,839 pixels), and 96.7% overall accuracy for the validation set of samples (18,249 pixels) (Figure 4B). In all of the analyses, the highest error rates were due to misclassification of pixels diagnosed as BOT by histopathology by Lasso as either normal or HGSC, while higher accuracy was observed for normal and HGSC classes (Supplemental Table 6). Interestingly, the same BOT samples misclassified by the two-class comparison between HGSC and BOT were also predicted as carcinomas by the three-class molecular model for normal, BOT and HGSC. These results emphasize that metabolic features detected by our method can serve as a robust predictive signature of cancer and disease aggressiveness.

To evaluate the overall discrimination between healthy and tumor samples, per-pixel results for HGSC and BOT were combined, and compared to the results for normal tissues. Overall agreements of 95.7% and 96.3% were achieved in the negative ion mode for the CV and validation sets, respectively (Figure 4A). Positive ion mode data also enabled successful discrimination between healthy and tumorous tissues with overall agreements of 94.8% for CV and 98.4% for the validation set (Figure 4B). The few normal pixels classified as HGSC were from samples NL_13 and 14, which presented higher stromal cell density compared to the remaining normal samples (Supplemental Table 2). Collectively, these results support lipid and metabolites profiles as predictive molecular features to distinguish healthy, borderline and aggressive serous ovarian cancers.

Molecular markers of ovarian cancer aggressiveness

Lasso analysis of normal, HGSCs and serous BOTs selected subsets of molecular features that were highly predictive and characteristic of disease state. An ion whose peak abundance is important for characterizing a certain class is given a positive weight, whereas ions whose low abundances or absence are important receive a negative weight. Note that trends of increased or decreased mass spectral relative abundance and 2D distributions in tissues were in agreement with the mathematical weight given by the Lasso for all of the selected molecular features. Figure 4C shows the statistical weights for the selected *m/z* values for the three-class normal, versus BOT, versus HGSC classification model, showing a high diversity of molecular species. Tentative chemical identification of the selected ions was performed using high mass accuracy/high mass resolution and tandem MS analyses in comparison to literature reports, lipids and metabolites databases, and chemical standards. Table 1 provides a list of the *m/z* values contributing to the model and the attributed weights, which were identified as 38 and 21 molecular species in the negative mode and positive ion mode, respectively. Attributed molecular formulas are included in Supplemental Table 7, with corresponding mass errors for each assigned *m/z* value. Similar *m/z* values were selected for the two-class molecular model for high-grade versus borderline tumors (Supplemental Table 5), supporting the potential role of those metabolic species as markers of tumor aggressiveness.

The selected molecular ions identified include metabolites, fatty acids, and complex lipids which play important biological roles. Within the small metabolites, gluconic acid (*m/z* 195.051) was given a positive weight for HGSC class and a negative weight for BOT class. Fragmentation patterns for *m/z* 195.051 and gluconic acid standard obtained with tandem MS analyses for structural confirmation as well as DESI-MS ion images are provided in Supplemental Figure 3. Interestingly, the non-oxidized form of gluconic acid, hexose or glucose (*m/z* 215.033), was observed in higher relative abundance in BOT tissues. An ion at *m/z* 174.041, identified as N-acetylaspartic acid (NAA), was selected as an important predictive feature for HGSC. Interestingly, NAA has been previously reported as a marker of normal brain parenchyma when compared to gliomas (29). Amino acid taurine and ascorbic acid were also selected as predictive markers of healthy ovarian tissues when compared to tumor tissue, both receiving positive weights for the normal tissue class. On the other hand, succinate and malate received negative weights for normal tissue class in comparison to serous ovarian tumors. Note that identification of metabolite species was performed using DESI-MS, tandem MS analyses in comparison to standards and literature reports, and high accuracy measurements (<1.7 ppm), although isomeric interferences at the same monoisotopic mass could still occur. Representative tandem MS spectra for the metabolites described are provided in Supplemental Figure 4.

Differences in fatty acid abundances and degree of saturation were also observed between the three tissue subtypes. Polyunsaturated fatty acids, such as FA 20:3 and FA 22:4 were given positive weights for characterizing the HGSC class. Interestingly, monounsaturated fatty acids FA 18:1 and FA 20:1 were given positive weights for characterizing serous BOTs, while saturated fatty acids (FA 16:0 and FA 18:0) and monoacylglycerol (MG 16:0) were given negative weights for serous BOTs. These results suggest fatty acid metabolism including their abundances and degree of saturation could play a role in serous ovarian tumor proliferation and aggressiveness, as previously shown for other cancers types (30,31).

Several GP species were also selected as important molecules in characterizing the three classes. In the negative ion mode, PG and PI species such as PG 16:0/18:1 or PI 18:0/18:1 received positive weights by the Lasso almost exclusively for HGSC classification. Positive weights for characterizing healthy ovarian tissue were obtained for PS species such as *m/z* 760.515 (PS 16:0/18:1). Furthermore, the molecular model built by the Lasso to discriminate between HGSC and healthy tissue (Supplemental Table 3) pinpointed additional GP markers such as CL. Positive weights were assigned to CL 72:8 and CL 72:7 to characterize HGSC, suggesting a role for these lipids in tumor growth and proliferation (32). In the positive ion mode, several PC species were selected as predictive markers. For example, several C32 PC species were given positive weights for characterization of HGSC class, while PC 34:1 received positive weight for healthy ovarian tissue. For BOT, several PC species received negative weights, while PC 36:2 provided positive correlations for characterizing the serous tumor subtype. The overall positive weights and increase in the relative abundances of PC species observed for HGSC class was in agreement with the positive weight attributed to *m/z* 104.107, identified as the choline head group. Notably, previous studies have also reported elevated levels for PC species in human epithelial ovarian cancer cells, which was related to tumor proliferation and differentiation (33,34). Representative tandem MS spectra for lipid species detected in the negative ion mode and positive ion mode are provided in Supplemental Figure 4 and Supplemental Figure 5, respectively.

Glycosphingolipids such as ceramides were also selected as predictive by our classification models. In the negative ion mode for example, Cer d42:3 and Cer d42:2 were given positive weights to characterize the healthy ovary class, while Cer d42:1 and Cer d34:1 received negative weights. On the other hand, Cer d34:1 and GlcCer d34:1 received positive weights for serous BOT tissue class, while Cer d34:2 received negative weights. In the positive ion mode, the SM 34:1 received a positive weight for the normal ovarian tissue class. Changes in glycosphingolipids expression have been previously reported in epithelial ovarian cancer by MALDI-MSI (35). These variations in ceramides in normal tissue and BOT present interesting insights to the disease, as different fatty-acid chain lengths of ceramide species have been associated to different functions in cancer pathogenesis (36).

Glycolipids such as TG presented high relative abundances in the mass spectra of both tumor subtypes, with distinctive chain lengths and saturation levels characteristic of HGSC and BOT. Sterol lipids such as CEs, which are important for cell membrane functionality, were selected as predictive markers of HGSC. For example, CE 20:4 was attributed a positive weight for HGSC class, while CE 18:2 received a negative weight. For the normal ovarian tissue class, CE 18:1 received a negative weight by the statistical model. The largest weight for the model was attributed to ubiquinone, the fully oxidized form of coenzyme Q, one of the electron carriers of the electron transfer chain that is used for ATP synthesis and cell signaling for proliferation (37). Ubiquinone presented notably increased relative abundances in tumorous areas in comparison to surrounding normal stroma (Figure 2), which suggests a potential role for this molecule as a marker for serous ovarian cancer.

Statistical prediction of intra-tumor heterogeneity

All of the previous analyses described were performed by comparing normal, BOT and HGSC pixels across tissue samples obtained from a total of 78 different patients. To evaluate our method performance in detecting tissue heterogeneity within the same patient tissue sample, we selected 5 HGSC samples that contained clear regions of stroma tissue adjacent to tumor within the same tissue section. Individual statistical classifiers were built for each patient using negative ion mode data. Lasso prediction results are presented in Supplemental Table 8. Excellent agreements with pathological classification were observed for all 5 patients (5,440 pixels), with an overall accuracy of 99.5% obtained for all patients combined. To visualize our method's performance in predicting heterogeneous tissue regions within the same tissue section, we plotted the statistical results for 4 patients analyzed, showing pixels classified as HGSC in red, and pixels classified as stroma in green (Figure 5). As observed, high spatial agreement between the predictive images and the pathologic diagnosis delineated in the optical images of the H&E stained sections was achieved.

Discussion

DESI-MS analysis of serous ovarian tumors allowed a detailed investigation of metabolic profiles characteristic of disease state and aggressiveness in the negative and positive ion modes. Different metabolic composition and relative abundances allowed clear identification of healthy ovarian tissues, HGSC, and serous BOT, within adjacent normal stroma and necrotic regions. DESI-MS imaging and pathological evaluation of the same tissue section was essential for study, allowing high specificity for selecting areas of interest and extracting molecular information for statistical evaluation. MS imaging enabled visualization of features within heterogeneous tumor regions, even for fine papillary branches present in serous BOT. This approach is powerful for investigating diagnostic molecular signatures as it accounts for cellular heterogeneity and thus increases the performance of the tissue-trained statistical classifiers. Here, we report an extensive investigation into the molecular profiles for HGSC and serous BOT, identifying metabolites, fatty acids and complex lipids as potential markers to discriminate aggressive and non-invasive tumors.

Alterations in the abundances of lipids and metabolites between healthy ovarian and tumorous serous tissues were detected by DESI-MS imaging, which reflect abnormalities in cancer cell metabolism. High relative abundance of ascorbic acid (vitamin C), a natural oxidant from dietary origin, was observed in normal ovarian tissue. The role of Vitamin C in maintaining proper functioning of the ovary has been previously described in the literature, such as for the development and survival of ovarian follicles (38). Several molecules were identified as important predictive markers of disease state and cancer aggressiveness, which may become important diagnostic markers and serve as novel targets for therapeutic approaches. Gluconic acid, a metabolite that connects the glucose and pentose phosphate pathways, was identified as a predictive marker for discrimination between HGSC and serous BOT, and is thus a possible marker of ovarian cancer aggressiveness. Remarkably, gluconic acid has been previously found to discriminate between stages pT2 and pT3 of prostate cancer (39). Succinate and malate, intermediates in the citric acid cycle, were also identified as predictive markers of serous ovarian cancers. The oncogenic activity of succinate has been previously reported and accumulation of malate has been shown to enhance fatty acid and cholesterol biosynthesis, enabling tumor growth (40).

Alterations in fatty acid and complex lipid metabolism were also detected by our approach. Previous studies have outlined the importance of fatty acid synthesis in tumor biology due to their ability to modulate the fluidity of lipid membranes and affect cellular machinery (41). Moreover, unsaturated fatty acids have been associated with clinically aggressive tumors, and were reported to stimulate the proliferation of human breast cancer cells, while saturated fatty acids induced cell death (30,31). Our results suggest that alterations in fatty acid unsaturation levels may play a role in serous ovarian cancer proliferation and aggressiveness. For example, polyunsaturated fatty acids, such as FA 20:3 and FA 22:4, were observed at high relative abundances in HGSC tissues and were given positive weights by the Lasso for this tissue class. To satisfy the high proliferating necessities of tumor cells, GPs are synthesized for continuous membrane production (42). During the review of this paper, a related study was published aiming to diagnose different types of epithelial ovarian cancer based on lipid profiles by DESI-MS (43). Our results show good agreement with some of the changes in GPs identified for normal and carcinoma differentiation, such as PS 36:1 and PS 34:1, which showcases the potential of DESI-MS as a robust tool for tissue characterization. In our study, several PG and PI species were identified as predictive markers for tumor aggressiveness, with increased relative abundance in HGSC samples. CLs, which are complex GP species present almost exclusively in the inner mitochondrial membrane, were also observed in increased relative abundances in HGSC tissue when compared to normal tissue (32). Moreover, increased relative abundances of ubiquinone, a component of the mitochondrial respiratory chain, was also found to be characteristic of serous ovarian tumors (37). Interestingly, mutations in mitochondrial DNA have been reported for human ovarian carcinomas, suggesting that alterations in mitochondria play a role in ovarian cancer tumorigenesis (44).

Another interesting group of lipid molecules identified as potential biomarkers by DESI-MS analysis were ceramides. Ceramides are sphingolipids which have been studied for their role in apoptosis, and have been found to be overexpressed in necrotic tissue (36,45). Here, we identified many ceramide species with different fatty acid chain lengths and saturation, which can help understand many of the underexplored biological functionalities of these molecules (36). LGSC, which evolve from BOTs, commonly present more chemoresistant responses than high-grade carcinomas (46). Notably, ceramides have been investigated for their role as potential biomarkers of chemotherapy response, and in this study, high relative abundances of ceramide species such as Cer d34:1 or GalCer d34:1 were characteristic of BOT (36). This finding could be of clinical importance, as it could help understand the mechanisms involved in chemotherapy response of serous carcinomas (4). Future studies will be pursued to investigate the biological pathways related to the expression of the molecules identified, which may help elucidate the pathogenesis of serous ovarian cancers and identify novel markers for early detection.

The classification models generated by the Lasso were successful in interpreting the large data sets, identifying molecular predictors of each tissue type as well as providing robust statistical classifiers. HGSC was classified with high accuracy in comparison to healthy stromal ovarian tissues, for both negative and positive ion mode data (96.4% overall agreement). Due to the recent findings proposing the distal end of the fallopian tube as the site of origin of HGSC (4), we plan to analyze fallopian tube molecular profiles to investigate the biological processes by which high-grade carcinoma initiates. A three-class classification model to differentiate between normal, BOT and HGSC was also built resulting in an overall agreement of 91.9% with pathologic evaluation. Overall, our method allowed discrimination between normal tissue and tumorous tissues including BOT and HGSC with 96.2% overall agreement.

Importantly, we also investigated predictive markers of tumor aggressiveness by directly comparing borderline and aggressive serous tumors using a two-class molecular model. Due to the contrasting biological pathways involved in BOT (which can develop to LGSC) and HGSC, both serous ovarian cancers were anticipated to entail distinct molecular features (4). The two-class classification models DESI-MS imaging data presented an overall accuracy of 93.0% in predicting HGSC and BOT, which demonstrates the clinical value of this technique in differentiating tumors with distinct invasive and aggressive behaviors. Remarkably, the three BOT samples misclassified as HGSC were re-evaluated by pathologic analysis and presented unusual histologic features associated with the development of low-grade carcinomas. The results suggest that changes in molecular composition detected by DESI-MS could be indicative of malignant behavior in borderline samples. We plan a follow up study to investigate more clinically relevant cases as well as to further explore the molecular mechanism of development from borderline to malignant tumors.

Proposed priorities to reduce ovarian cancer incidence and improve patient outcome include the identification of biomarkers for prevention and early disease detection and the development of an integrated molecular view of the disease (7,47,48). Our results suggest that DESI-MS addresses these concerns by providing molecular information of a diverse group of lipids and metabolites that can serve as potential new markers of serous ovarian cancer. Moreover, predictive markers of HGSC and BOT tumors were identified which may be used for the development of new therapeutic targets and preventive screening. Importantly, the ease and speed by which diagnostic molecular information can be obtained by DESI-MS and other relative ambient ionization techniques makes this technology attractive for clinical use (49). Thus, we suggest DESI-MS as a potential clinical technology to integrate metabolic markers with clinical and pathological approaches to provide more accurate tissue diagnosis and improve management of serous ovarian cancer patients.

Supplementary Material

Refer to Web version on PubMed Central for supplementary material.

Acknowledgments

This work was supported by the NIH/NCI (R00CA190783, P50 CA083639), The Welch Foundation (grant F-1895), and the American Cancer Society Research Professor Award. We thank AnneClaire Wageman and John Lin for assistance with experiments and statistical analysis, and Dr. Emily L. Que for providing use of the light microscopy imaging system. Tissue samples were provided by the MD Anderson Cancer Center Tissue Bank, and the Cooperative Human Tissue Network which is funded by the NCI.

Financial support:

This work was supported by the NIH/NCI (grant R00CA190783 to L.S. Eberlin, grant P50 CA083639 to A.K. Sood), The Welch Foundation (grant F-1895 to L.S. Eberlin), and the American Cancer Society Research Professor Award to A.K. Sood.

References

1. Rosen DG, Zhang Z, Shan W, Liu J. Morphological and molecular basis of ovarian serous carcinoma. J Biomed Res. 2010; 24(4):257–63. [PubMed: 23554638]
2. Bowtell DDL. The genesis and evolution of high-grade serous ovarian cancer. Nat Rev Cancer. 2010; 10(11):803–08. [PubMed: 20944665]
3. Leong HS, Galletta L, Etemadmoghadam D, George J, Kobel M, Ramus SJ, et al. Efficient molecular subtype classification of high-grade serous ovarian cancer. Journal of Pathology. 2015; 236(3):272–77. [PubMed: 25810134]
4. Vang R, Shih IM, Kurman RJ. Ovarian Low-grade and High-grade Serous Carcinoma Pathogenesis, Clinicopathologic and Molecular Biologic Features, and Diagnostic Problems. Adv Anat Pathol. 2009; 16(5):267–82. [PubMed: 19700937]
5. Hart WR. Borderline epithelial tumors of the ovary. Modern Pathol. 2005; 18:S33–S50.

6. Fischerova D, Zikan M, Dundr P, Cibula D. Diagnosis, Treatment, and Follow-Up of Borderline Ovarian Tumors. Oncologist. 2012; 17(12):1515–33. [PubMed: 23024155]
7. Vaughan S, Coward JI, Bast RC, Berchuck A, Berek JS, Brenton JD, et al. Rethinking ovarian cancer: recommendations for improving outcomes. Nat Rev Cancer. 2011; 11(10):719–25. [PubMed: 21941283]
8. Zhu JJ, Djukovic D, Deng LL, Gu HW, Himmati F, Abu Zaid M, et al. Targeted serum metabolite profiling and sequential metabolite ratio analysis for colorectal cancer progression monitoring. Analytical and Bioanalytical Chemistry. 2015; 407(26):7857–63. [PubMed: 26342311]
9. Konstantinopoulos PA, Spentzos D, Karlan BY, Taniguchi T, Fountzilas E, Francoeur N, et al. Gene Expression Profile of BRCAness That Correlates With Responsiveness to Chemotherapy and With Outcome in Patients With Epithelial Ovarian Cancer. Journal of Clinical Oncology. 2010; 28(22): 3555–61. [PubMed: 20547991]
10. Saad AF, Hu W, Sood AK. Microenvironment and pathogenesis of epithelial ovarian cancer. Horm Cancer. 2010; 1(6):277–90. [PubMed: 21761359]
11. Zeppernick F, Ardighieri L, Hannibal CG, Vang R, Junge J, Kjaer SK, et al. BRAF Mutation Is Associated With a Specific Cell Type With Features Suggestive of Senescence in Ovarian Serous Borderline (Atypical Proliferative) Tumors. American Journal of Surgical Pathology. 2014; 38(12): 1603–11. [PubMed: 25188864]
12. Chughtai K, Heeren RMA. Mass Spectrometric Imaging for Biomedical Tissue Analysis. Chemical Reviews. 2010; 110(5):3237–77. [PubMed: 20423155]
13. Fletcher JS, Vickerman JC, Winograd N. Label free biochemical 2D and 3D imaging using secondary ion mass spectrometry. Current Opinion in Chemical Biology. 2011; 15(5):733–40. [PubMed: 21664172]
14. Norris JL, Caprioli RM. Analysis of Tissue Specimens by Matrix-Assisted Laser Desorption/ Ionization Imaging Mass Spectrometry in Biological and Clinical Research. Chemical Reviews. 2013; 113(4):2309–42. [PubMed: 23394164]
15. Wiseman JM, Ifa DR, Song QY, Cooks RG. Tissue imaging at atmospheric pressure using desorption electrospray ionization (DESI) mass spectrometry. Angew Chem Int Edit. 2006; 45(43): 7188–92.
16. Venter A, Sojka PE, Cooks RG. Droplet dynamics and ionization mechanisms in desorption electrospray ionization mass spectrometry. Anal Chem. 2006; 78(24):8549–55. [PubMed: 17165852]
17. Eberlin LS, Ferreira CR, Dill AL, Ifa DR, Cooks RG. Desorption electrospray ionization mass spectrometry for lipid characterization and biological tissue imaging. Biochim Biophys Acta. 2011; 1811(11):946–60. [PubMed: 21645635]
18. Eberlin LS, Norton I, Dill AL, Golby AJ, Ligon KL, Santagata S, et al. Classifying human brain tumors by lipid imaging with mass spectrometry. Cancer Res. 2012; 72(3):645–54. [PubMed: 22139378]
19. Guenther S, Muirhead LJ, Speller AV, Golf O, Strittmatter N, Ramakrishnan R, et al. Spatially resolved metabolic phenotyping of breast cancer by desorption electrospray ionization mass spectrometry. Cancer Res. 2015; 75(9):1828–37. [PubMed: 25691458]
20. Eberlin LS, Tibshirani RJ, Zhang J, Longacre TA, Berry GJ, Bingham DB, et al. Molecular assessment of surgical-resection margins of gastric cancer by mass-spectrometric imaging. Proc Natl Acad Sci U S A. 2014; 111(7):2436–41. [PubMed: 24550265]
21. Eberlin LS, Dill AL, Costa AB, Ifa DR, Cheng L, Masterson T, et al. Cholesterol Sulfate Imaging in Human Prostate Cancer Tissue by Desorption Electrospray Ionization Mass Spectrometry. Analytical Chemistry. 2010; 82(9):3430–34. [PubMed: 20373810]
22. Dill AL, Eberlin LS, Zheng C, Costa AB, Ifa DR, Cheng LA, et al. Multivariate statistical differentiation of renal cell carcinomas based on lipidomic analysis by ambient ionization imaging mass spectrometry. Analytical and Bioanalytical Chemistry. 2010; 398(7–8):2969–78. [PubMed: 20953777]
23. Dill AL, Eberlin LS, Costa AB, Zheng C, Ifa DR, Cheng LA, et al. Multivariate Statistical Identification of Human Bladder Carcinomas Using Ambient Ionization Imaging Mass Spectrometry. Chem-Eur J. 2011; 17(10):2897–902. [PubMed: 21284043]

24. Paine MRL, Kim J, Bennett RV, Parry RM, Gaul DA, Wang MD, et al. Whole Reproductive System Non-Negative Matrix Factorization Mass Spectrometry Imaging of an Early-Stage Ovarian Cancer Mouse Model. Plos One. 2016; 11(5)
25. Tibshirani R. Regression shrinkage and selection via the Lasso. Journal of the Royal Statistical Society Series B-Methodological. 1996; 58(1):267–88.
26. Friedman J, Hastie T, Tibshirani R. Regularization Paths for Generalized Linear Models via Coordinate Descent. J Stat Softw. 2010; 33(1):1–22. [PubMed: 20808728]
27. Eberlin LS, Ferreira CR, Dill AL, Ifa DR, Cooks RG. Desorption electrospray ionization mass spectrometry for lipid characterization and biological tissue imaging. Biochimica Et Biophysica Acta-Molecular and Cell Biology of Lipids. 2011; 1811(11):946–60.
28. Powers S, Hastie T, Tibshirani R. Customized Training with an Application to Mass Spectrometric Imaging of Cancer Tissue. Ann Appl Stat. 2015; 9(4):1709–25.
29. Jarmusch AK, Pirro V, Baird Z, Hattab EM, Cohen-Gadol AA, Cooks RG. Lipid and metabolite profiles of human brain tumors by desorption electrospray ionization-MS. P Natl Acad Sci USA. 2016; 113(6):1486–91.
30. Hardy S, El-Assaad W, Przybytkowski E, Joly E, Prentki M, Langelier Y. Saturated fatty acid-induced apoptosis in MDA-MB-231 breast cancer cells - A role for cardiolipin. J Biol Chem. 2003; 278(34):31861–70. [PubMed: 12805375]
31. Kuhajda FP. Fatty-acid synthase and human cancer: New perspectives on its role in tumor biology. Nutrition. 2000; 16(3):202–08. [PubMed: 10705076]
32. Zhang J, Yu W, Ryu S, Lin J, Buentello G, Tibshirani R, et al. Cardiolipins are biomarkers of mitochondria-rich thyroid oncocytic tumors. Cancer Res. 2016
33. Iorio E, Ricci A, Bagnoli M, Pisanu ME, Castellano G, Di Vito M, et al. Activation of phosphatidylcholine cycle enzymes in human epithelial ovarian cancer cells. Cancer Res. 2010; 70(5):2126–35. [PubMed: 20179205]
34. Bagnoli M, Granata A, Nicoletti R, Krishnamachary B, Bhujwalla ZM, Canese R, et al. Choline Metabolism Alteration: A Focus on Ovarian Cancer. Front Oncol. 2016; 6
35. Liu Y, Chen Y, Momin A, Shaner R, Wang E, Bowen NJ, et al. Elevation of sulfatides in ovarian cancer: an integrated transcriptomic and lipidomic analysis including tissue-imaging mass spectrometry. Mol Cancer. 2010; 9:186. [PubMed: 20624317]
36. Saddoughi SA, Ogretmen B. Diverse functions of ceramide in cancer cell death and proliferation. Adv Cancer Res. 2013; 117:37–58. [PubMed: 23290776]
37. Ernster L, Dallner G. Biochemical, physiological and medical aspects of ubiquinone function. Biochim Biophys Acta. 1995; 1271(1):195–204. [PubMed: 7599208]
38. Devine PJ, Perreault SD, Luderer U. Roles of Reactive Oxygen Species and Antioxidants in Ovarian Toxicity. Biol Reprod. 2012; 86(2)
39. Jung K, Reszka R, Kamlage B, Bethan B, Stephan C, Lein M, et al. Tissue metabolite profiling identifies differentiating and prognostic biomarkers for prostate carcinoma. Int J Cancer. 2013; 133(12):2914–24. [PubMed: 23737455]
40. Gaude E, Frezza C. Defects in mitochondrial metabolism and cancer. Cancer Metab. 2014; 2:10. [PubMed: 25057353]
41. Baenke F, Peck B, Miess H, Schulze A. Hooked on fat: the role of lipid synthesis in cancer metabolism and tumour development. Dis Model Mech. 2013; 6(6):1353–63. [PubMed: 24203995]
42. Hutschenreuther A, Birkenmeier G, Bigl M, Krohn K, Birkemeyer C. Glycerophosphoglycerol, Beta-alanine, and pantothenic Acid as metabolic companions of glycolytic activity and cell migration in breast cancer cell lines. Metabolites. 2013; 3(4):1084–101. [PubMed: 24958267]
43. Doria ML, McKenzie JS, Mroz A, Phelps DL, Speller A, Rosini F, et al. Epithelial ovarian carcinoma diagnosis by desorption electrospray ionization mass spectrometry imaging. Sci Rep-Uk. 2016:6.
44. Liu VW, Shi HH, Cheung AN, Chiu PM, Leung TW, Nagley P, et al. High incidence of somatic mitochondrial DNA mutations in human ovarian carcinomas. Cancer Res. 2001; 61(16):5998–6001. [PubMed: 11507041]

45. Alessandra Tata MW, Ventura Manuela, Bernards Nicholas, Ganguly Milan, Gribble Adam, Shrestha Bindesh, Bluemke Emma, Ginsberg Howard J, Vitkin Alex, Zheng Jinzi. Arash Zarrine-AfsarDetection of Necrosis in Breast Cancer with Desorption Electrospray Ionization Mass Spectrometry. Sci Rep-Uk. 2016; 6(35374)
46. Gershenson DM, Sun CC, Bodurka D, Coleman RL, Lu KH, Sood AK, et al. Recurrent low-grade serous ovarian carcinoma is relatively chemoresistant. Gynecol Oncol. 2009; 114(1):48–52. [PubMed: 19361839]
47. Bowtell DD, Bohm S, Ahmed AA, Aspuria PJ, Bast RC, Beral V, et al. Rethinking ovarian cancer II: reducing mortality from high-grade serous ovarian cancer. Nat Rev Cancer. 2015; 15(11):668–79. [PubMed: 26493647]
48. Nick AM, Coleman RL, Ramirez PT, Sood AK. A framework for a personalized surgical approach to ovarian cancer. Nat Rev Clin Oncol. 2015; 12(4):239–U78. [PubMed: 25707631]
49. Ifa DR, Eberlin LS. Ambient Ionization Mass Spectrometry for Cancer Diagnosis and Surgical Margin Evaluation. Clinical Chemistry. 2016; 62(1):111–23. [PubMed: 26555455]

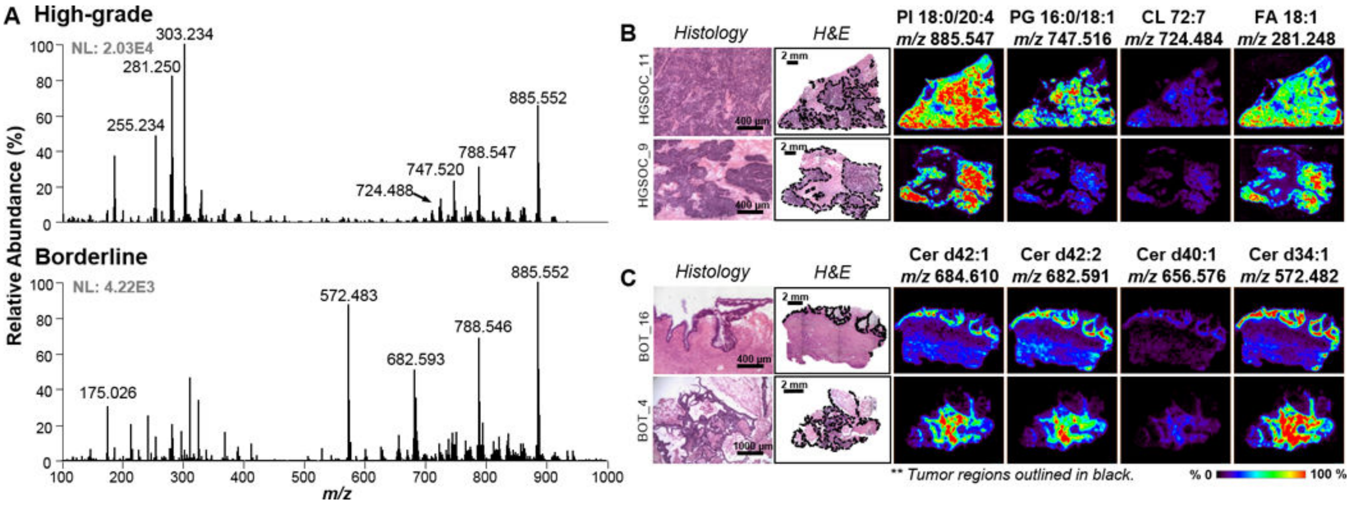

Figure 1.

Analysis by DESI-MSI in the negative ion mode. A) Representative metabolic profiles for high-grade SOC and serous borderline. Top: High-grade. Bottom: Borderline B) Representative ion images for high-grade SOC tissue samples. C) Representative ion images for borderline tumor samples. Tumor areas are outlined in black on H&E slides. Areas of red intensity within the ion images represent highest (100%) and black lowest (0%) relative abundances. PI: glycerophosphoinositol PG: glycerophosphoglycerol CL: cardiolipin FA: fatty acid Cer: Ceramide. Lipid species are described by number of fatty acid chain carbons and double bonds.

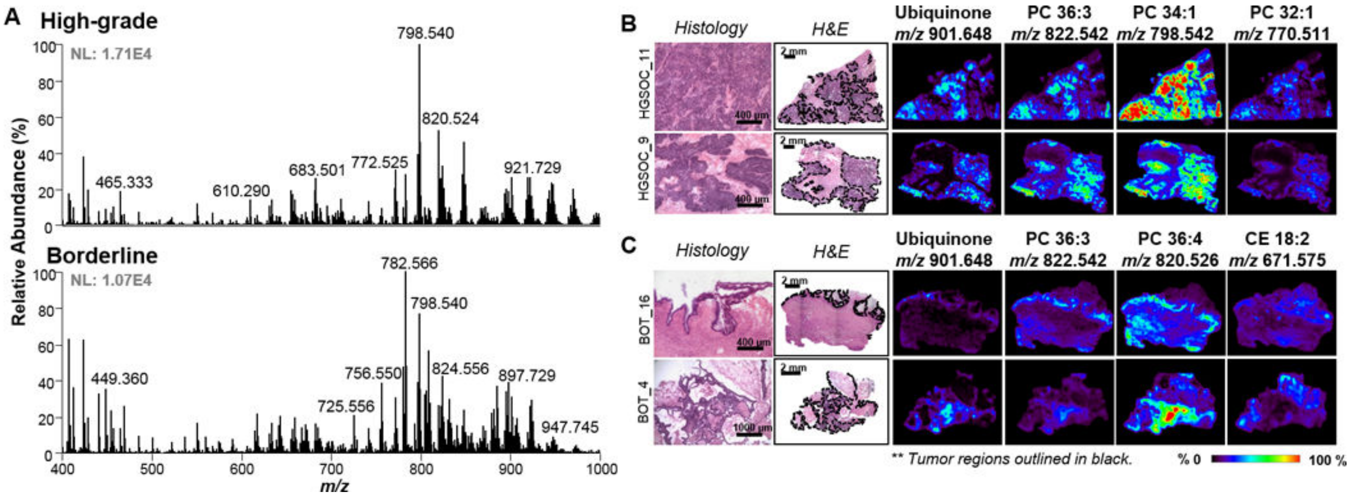

Figure 2.

Analysis by DESI-MSI in the positive ion mode. A) Representative metabolic profiles for high-grade SOC and serous borderline. Top: High-grade. Bottom: Borderline B) Representative ion images for high-grade SOC tissue samples. C) Representative ion images for borderline tumor samples. Tumor areas are outlined in black on H&E slides. Areas of red intensity within the ion images represent highest (100%) and black lowest (0%) relative abundances. Adjacent tissue sections were used for negative and positive ion mode analysis. PC: glycerophosphocholine CE: cholesteryl ester. Lipid species are described by number of fatty acid chain carbons and double bonds.

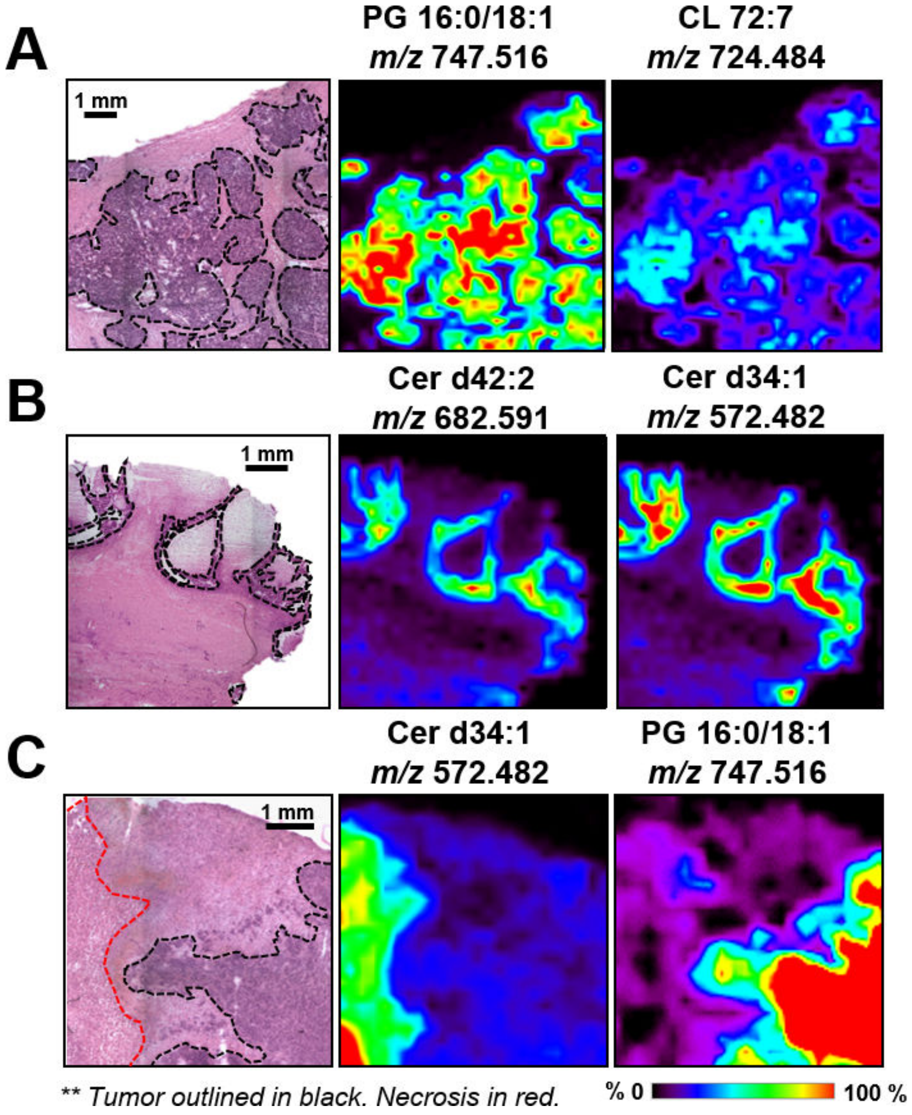

Figure 3.

Magnified regions for samples A) HGSC_11 B) BOT_16 C) HGSC_1; with selected ion images that correlate to and outline the presented histological heterogeneities. PG: glycerophosphoglycerols. Cer: Ceramide. Lipid species are described by number of fatty acid chain carbons and double bonds. The tumor areas are outlined in black, necrotic areas in red. Areas of red intensity within the ion images represent highest (100%) and black lowest (0%) relative abundances.

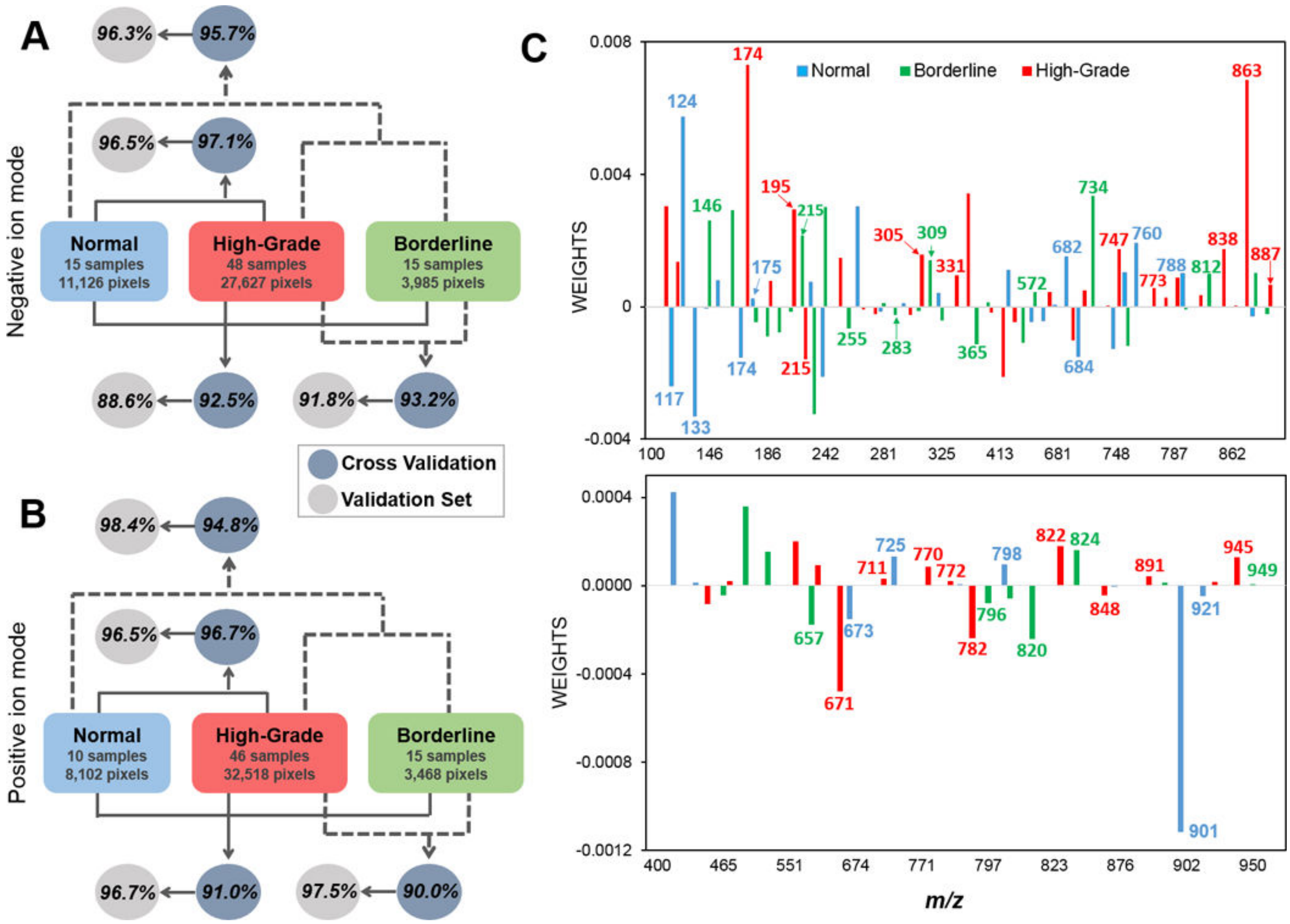

Figure 4.

Lasso per pixel prediction results for normal, HGSC and BOT classification. A) Negative ion mode B) Positive ion mode. Agreements are calculated based on percentage of correctly classified pixels over total pixels classified. See Supplemental Table 2, 4, and 6 for complete pixel and patient classification results. C) Weights attributed to selected *m/z* values by the Lasso, represented by nominal mass, for negative ion mode (top) and positive ion mode (bottom). Positive weights represent higher relative abundances; negative weights represent lower relative abundances. Chemical attribution for selected species is provided in Table 1.

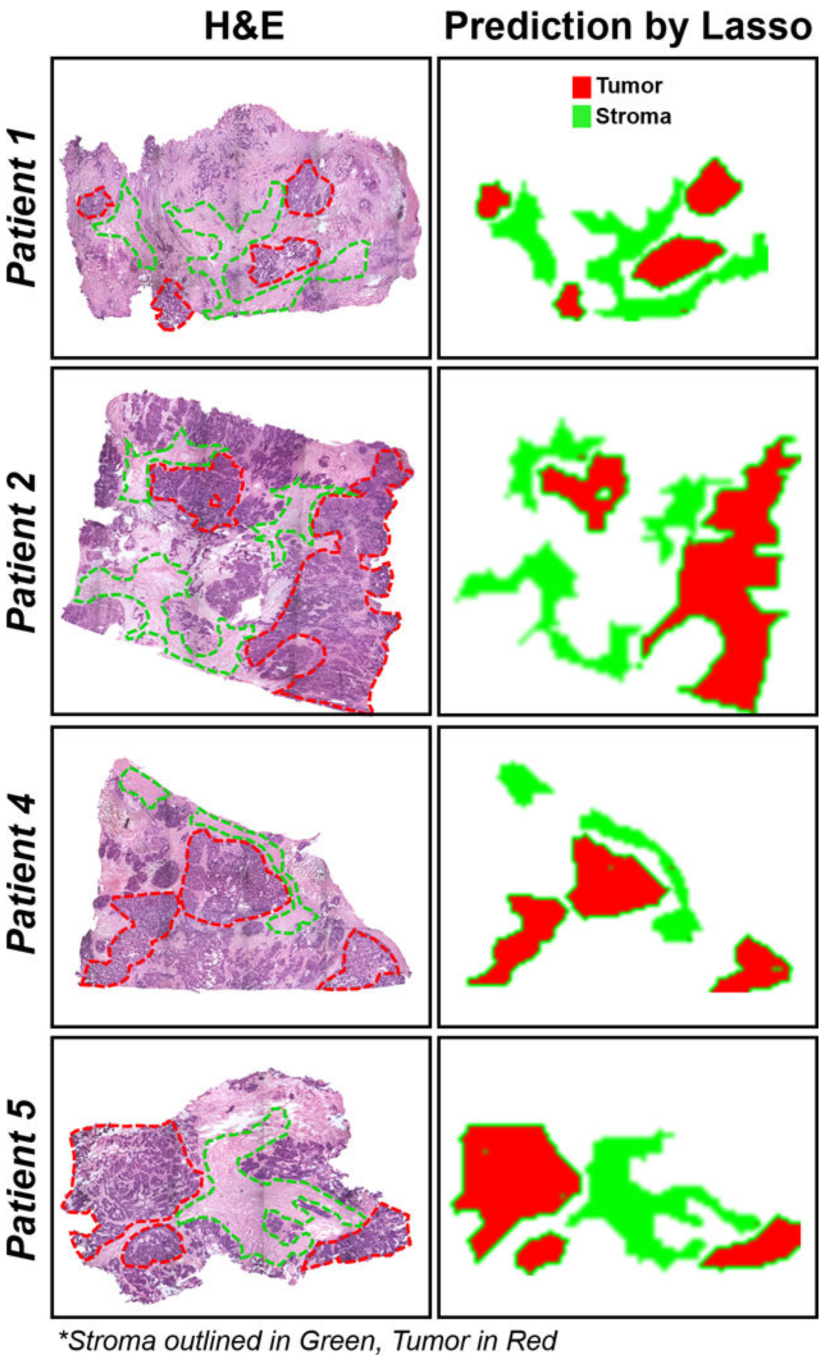

Figure 5.

Prediction images of tumor and stroma tissue regions by the Lasso for 4 HGSC patients. Regions of tumor (red) and stroma (green) are outlined on the optical images of H&E stained tissues in the left column. The right column shows the corresponding predictions by the Lasso for the areas selected.

Table 1

Identified species selected by the Lasso as significant contributors to the molecular model for normal, borderline and high-grade SOC classification with attributed statistical weights. Chemical species were tentatively identified by high mass accuracy/high mass resolution and tandem MS analyses. Positive weights represent higher relative abundances; negative weights represent lower relative abundances. Double negative and double positives correspond to greater contributions to the model. Negative ion mode: Lasso weights: ‘++’ ‘− −’ ≥ │0.001│; ‘+’ ‘−’ < │0.001│. Positive ion mode: Lasso weights: ‘++’ ‘− −’ ≥ │0.0001│; ‘+’ ‘−’ < │0.0001│. Molecular formulas and mass errors are provided in Supplemental Table 7. Representative tandem mass spectra for selected m/z species are provided in Supplemental Figs. 3–5.

NEGATIVE ION MODE				
Attribution	**Weights by Lasso**			**Detected m/z**
	Normal	**Borderline**	**High-Grade**	
Succinate	− −		++	117.020
Taurine	++			124.008
Malate	− −			133.014
Glutamic acid	−	++		146.046
N-acetylaspartic acid	− −		++	174.041
Ascorbic acid	+	−		175.025
Gluconic acid		−	++	195.051
Hexose		++	− −	215.033
Phosphatidic acid	+	− −		226.996
FA 16:0		−		255.233
FA 18:2			−	279.233
FA 18:1	−	+		281.248
FA 18:0		−		283.264
FA 20:4	+		−	303.233
FA 20:3		−	++	305.248
FA 20:1		++		309.280
FA 22:4			+	331.264
MG 16:0		− −		365.246
Cer d34:2		− −		570.466
Cer d34:1	−	+		572.481
Cer d42:3	+			680.575
Cer d42:2	++		−	682.590
Cer d42:1	− −		+	684.607
GlcCer d34:1		++		734.535
PE 36:2			+	742.538
PG 16:0/18:1	− −		++	747.520
PS 16:0/18:1	++			760.515
PG 18:1/18:1			+	773.533
PG 18:0/18:1			+	775.548
PS 18:1/18:1 or 18:0/18:2			+	786.528

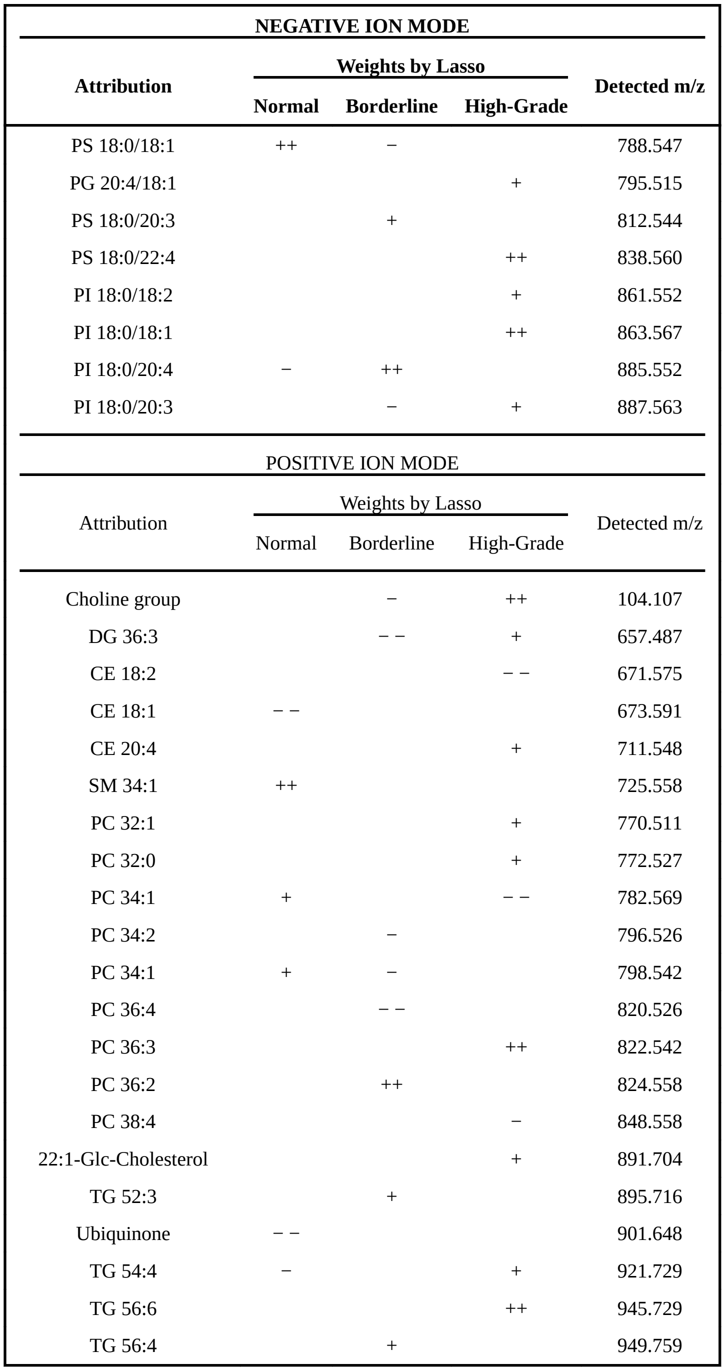

NEGATIVE ION MODE

Attribution	**Weights by Lasso**			**Detected m/z**
	Normal	**Borderline**	**High-Grade**	
PS 18:0/18:1	++	−		788.547
PG 20:4/18:1			+	795.515
PS 18:0/20:3		+		812.544
PS 18:0/22:4			++	838.560
PI 18:0/18:2			+	861.552
PI 18:0/18:1			++	863.567
PI 18:0/20:4	−	++		885.552
PI 18:0/20:3		−	+	887.563

POSITIVE ION MODE

Attribution	Weights by Lasso			Detected m/z
	Normal	Borderline	High-Grade	
Choline group		−	++	104.107
DG 36:3		− −	+	657.487
CE 18:2			− −	671.575
CE 18:1	− −			673.591
CE 20:4			+	711.548
SM 34:1	++			725.558
PC 32:1			+	770.511
PC 32:0			+	772.527
PC 34:1	+		− −	782.569
PC 34:2		−		796.526
PC 34:1	+	−		798.542
PC 36:4		− −		820.526
PC 36:3			++	822.542
PC 36:2		++		824.558
PC 38:4			−	848.558
22:1-Glc-Cholesterol			+	891.704
TG 52:3		+		895.716
Ubiquinone	− −			901.648
TG 54:4	−		+	921.729
TG 56:6			++	945.729
TG 56:4		+		949.759